Electrochemical nanobiosensor for real-time detection of gap junction-mediated intercellular communication activity

Halina V. Grushevskaya[1], Nina G. Krylova[1*], Igor V. Lipnevich[1], Taisija I. Orekhovskaja[2], Boris G. Shulitski[2]

[1]*Belarusian State University, 4 Nezavisimosti Ave., Minsk, 220030, Belarus*
[2]*Belarusian State University of Informatics and Radioelectronics, 6 P. Brovki Str., Minsk, 220013, Belarus*

[*]Corresponding author. Tel: (+375) 172095081; Fax: (+375) 172095445; E-mail: krylovang@bsu.by

Received: 10 September 2016, Revised: 17 October 2016 and Accepted: 20 November 2016

DOI: 10.5185/amlett.2017.7092
www.vbripress.com/aml

Abstract

A capacitive nanobiosensor which consists of multiwalled carbon nanotubes (MWCNTs) covered by conducting oligomer of thiophene-pyrrole derivatives was constructed and fabricated to detect the gap junction-mediated communication between living cells in a monolayer. The sensor operates on screening and spin-dependent polarization effects in nanoheterostructures which present themselves MWCNTs decorated by organometallic complexes of high-spin Fe(II) and are fabricated by a Langmuir-Blodgett (LB) technique. The nanoheterostructures were deposited on transducer, which is an interdigital electrode system covered by a dielectric layer. As the cell monolayer density increased while the cells proliferated on the sensor surface, the sensor capacity decreased until the cell monolayer was confluent. This decrement is due to a forming network of the open gap junction channels (GJCs) in accordance with an electrochemical analysis performed. The monolayer capacity increases when adding GJC inhibitor (carbenoxolone) which leads to decrease of a number of the open GJCs. The technique has been used in real-time regime to establish some principles of menadione-mediated GJC-network fine-tuning. Menadione causes Ca^{2+}-dependent GJ channels opening/closing.

Keywords: Impedance analysis; intercellular communication; gap junction channel; nanobiosensor.

Introduction

Unique properties of carbon nanomaterials can be suppressed by adsorbed atoms and ions **[1**, **2]**. Therefore, decorating of carbon nanotubes, polymers and graphene-like monolayers to improve the electronic, optical performances is a challenge. For biosensorics is also important to maintain the high redox ability of an electrochemical transducer in the presence of halogen ions (Cl, I, Br). Graphene-like monoatomic layers (for example, graphitic carbon nitride monolayer) enhance the performances and redox ability by halogen ions with low coverage rate while suppressed by carbon atoms **[3]**. In order to improve the electroactivity and redox ability of the conducting polymers, molecules containing conjugated system can be used, for example, 2,5-di-(2-thienyl)-pyrrole **[4]**. Label-free impedance analysis can provide real-time and non-invasive observations of cellular response to various stimuli. Construction of electroactive nanobiosensors with redox ability would allow to study redox systems of living cells, for example, redox systems, which provide intercellular communication.

Gap junction-mediated intercellular communication is significant for maintenance of tissue homeostasis, while disruptions of gap junction channels (GJCs) are associated with some pathological states, including cancer. Investigations of cooperative dynamics of living cell monolayer have shown that there exists a dynamical network of GJCs, which penetrate cellular membranes **[5-9]**. Formation of the communicative gap junction channel network (CGJC network) occurs in the result of both self-assembly/self-disassambly of individual GJC and establishment of bistable channels in a given state: "open" or "closed". The process of self-assembly/self-disassembly has been studied a lot, and GJC inhibitors were found. However, the establishing of threshold signal transduction principles for opening/closing of GJCs in the gap junction network is the challenge because of multifactor and complicated signaling pathways with large number of regulatory molecules **[10]**. To date, the measurement of gap junction intercellular communication (GJIC) are carried out by using a number of methods, such as dye transfer through microinjection, the scrape/scratch loading, electroporation, gap-FRAP (fluorescence recovery after photobleaching), local activation of molecular fluorescent probe (LAMP), or by

measuring electrical conductance utilizing dual-patch clamp **[11]**. Microinjection of membrane-impermeable, nontoxic tracers into single cells has been the most commonly used technique for identifying GJIC. This method allows to reveal the correlation of morphological and functional data from individual cells as well as to give quantitative information about the transfer rate from one cell to another, permitting the comparison of CGJC network activity in different cell types. However, the microinjection technique possesses serious limitations: it requires specialized sophisticated and expensive equipment; the amount of microinjected tracer is difficult to standardize; there is a problem in discriminating stained from unstained (autofluorescent) cells; and microinjection is unsuitable for detecting early cellular responses and effects that require a repetitive stimulation of cells **[11]**. The dual patch clamp technique is a powerful method for quantitative determination of junctional conductance. However, it is slow, labor-intensive, and expensive method, while measurements by means of patch clamp technique can give considerable errors due to series resistance problems. Thus, the development of new advanced methods of CGJC network activity detection is highly on demand for modern cell biology.

Any signal of living cell leads to change of potential difference on the boundary living cell/physiological medium. It is known **[12**, **13]** that an impedance analysis allows to detect capacity of a double electrically charged layer and, respectively, dielectric polarization in it, for example, to study membrane polarization of living cells in suspension (see, for example, **[14]**). Electrical cell-substrate impedance sensing (ECIS) is a label-free and non-invasive technology which is a powerful tool to study cellular properties and functioning in real-time. ECIS measurements have been successfully used to monitor cell proliferation, motility, attachment and spreading, to evaluate cytotoxicity of biochemical compounds **[15**, **16]**. So, to date, the investigations of GJIC have been performed by methods which require labeling, and by techniques that alters cell activity. Current impedance analysis methods enable low-frequency monitoring of cell-cell tight junctions formation, but not CGJC network activity.

Electrode coatings consisting of nanocomposites of carbon nanotubes or gold nanoparticles have significantly improved sensitivity of electrochemical sensors for studies of cancer cells **[17]**. The improved sensitivity was attributed to increased surface roughness and intensification of cell interaction with substrate. From the other hand, the use of special coatings, for example conducting polymers, can result in much higher sensitivity of electrochemical sensors due to their unique physicochemical properties **[18]**. Biocompatible graphene-like materials with high conductance and large spin relaxation times for charged carrier density are perspective transducers **[19]**. The use of carbon nanotubes (CNT) or graphene as sensitive elements is hampered due to the lack of free charge carriers at the Fermi level in these materials **[20-22]**. However, when the materials were decorated with metal atoms, one can obtain an excitonic dielectric with non-zero electric charge density at the Fermi level **[1-2]**.

In this paper we utilize the LB technique to fabricate new biocompatible layered nanoheterostructures consisting of multi-walled CNT (MWCNT) bundles, which have been deposited on ultrathin LB-films of organometallic compounds. An electrochemical technique to detect functional changes proceeding in living cell monolayers immediately after their stimulation or inhibition, has been developed in **[23**, **24]**. This present work is motivated by the desire to develop a non-invasive and sensitive tool based on impedance analysis to detect GJIC.

In our paper, the technique will be used to demonstrate that GJCs opening results in decrease of the sensor capacity and to establish principles of CGJC-network fine-tuning. Understanding of these principles would allow to program the CGJC network and, hence, to correct of pathological states. We will construct capacitive nanobiosensor based on metal-containing conducting polymer / MWCNT LB-films to detect the GJC response to redox-active compound (menadione) affect on cells in a monolayer.

The goal is to reveal quantum polarization effects on interface between water and nanoheterostructures based on MWCNT bundles decorated by organometallic complexes of high-spin Fe(II), and to develop a sensor that functions based on these effects and detects interface polarization in a gap junction network of a living cell monolayer.

Experimental

Reagents

MWCNTs with diameters ranging from 2.0 to 5 nm and length of ~2.5 μm were obtained by the method of chemical vapor deposition (CVD-method) **[25]**. MWCNTs were covalently modified by carboxyl groups and non-covalently functionalized by stearic acid molecules. Salts $Fe(NO_3)_3 \cdot 9H_2O$, $Ce_2(SO_4)_3$ (Sigma, USA), hydrochloric acid, deionized water were used to preparate subphases. Iron-containing films were fabricated from an amphiphilic oligomer of thiophene-pyrrole derivatives with chemically bounded hydrophobic 16-link hydrocarbon chain: 3-hexadecyl-2,5-di(2-thienyl)-1H-pyrrole (H-DTP, H-dithienylpyrrole), chemical structure of which is shown in **Fig. 1**. H-dithienylpyrrole was synthesized by a method proposed in **[26]**. Working solution of H-dithienylpyrrole, $1.0 \cdot 10^{-3}$ M, was prepared by dissolving precisely weighed substances in hexane. All salt solutions have been prepared with deionized water with resistivity 18.2 MΩ·cm. Menadione and GJC inhibitor carbenoxolone sodium sald (CSS) (Sigma, USA) were utilized to alter cellular communication activity. Propidium iodide (Life Technologies, USA) was used to evaluate cell viability. All used materials belong to class of analytical pure reagents.

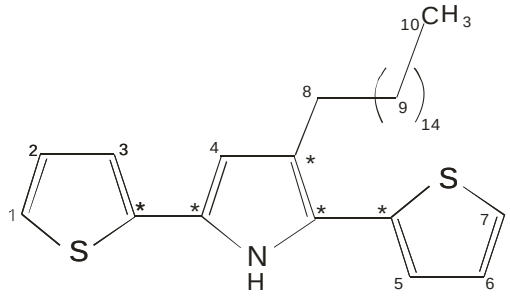

Fig. 1. Chemical structure of H-dithienylpyrrole molecule. Numbers and symbol * denote atoms C bounded with H, and without H, respectively.

Cell culture, morphology, and viability

C6 cell line from rat (rat C6 glioma) obtained from culture collection of Institute of Epidemiology and Microbiology (Minsk, Belarus) were grown on aligned MWCNT arrays and Fe-containing LB-DTP-films in a Dulbecco's modified Eagle medium (DMEM) (Sigma, USA) supplemented with 10 % fetal bovine serum and $1.0 \cdot 10^{-4}$ g/ml gentamycin at 37 °C in a humidified 5 % CO_2 atmosphere. Cells were photographed with a confocal light microscope and/or the cells were stained by propidium iodide (PI) and their viability was determined by scanning fluorescent microscopy (Nanofinder HE, "LOTIS-TII", Tokyo, Japan–Belarus).

Methods

Langmuir–Blodgett technique

Langmuir - Blodgett monolayer formation was carried out on an automated hand-made Langmuir trough with controlled deposition on a substrate, and with computer user interface working under Microsoft Windows operational system. Control of the surface tension has been performed by a highly sensitive resonant inductive sensor. The Y-type transposition of monolayers on supports was performed by their vertical dipping. The complexes Fe(II)DTP_3 of high-spin Fe(II) with the dithienylpyrrole ligands were synthesized by the LB-technique at compression of H-dithienylpyrrole molecules on the surface of subphase with salts of three-valence Fe **[27-29]**. Horizontally and vertically arranged LB-MWCNT-bundles can be fabricated from the multi-walled CNTs **[30]**. We utilize the Langmuir–Blodgett technique to fabricate new biocompatible layered nanoheterostructures consisting of two MWCNT LB-monolayers which are deposited on five-monolayer LB-film of the organometallic complexes, as shown in **Fig. 2c**.

Impedance measurements

For electrochemical studies, we use a planar capacitive sensor of interdigital-type on pyroceramics support. *N* pairs, *N*=20, of aluminum electrodes of the sensors in **Fig. 2a** are arranged in an Archimedes-type spiral configuration. Every such a pair is an "open type" capacitor. Dielectric coating of the electrodes represents itself nanoporous anodic alumina layer (AOA) with a pore diameter of 10 nm. The obtained LB-nanoheterostructures were suspended on the interdigital electrode system covered by dielectric AOA. The sensor was placed into aqueous salt solutions, or culture medium, or deionized water. A double electrically charged layer forms on the interface, as it is shown in **Fig. 2b**. A living cell monolayer was grown on the nanoheterostructures in **Fig. 2c-d**.

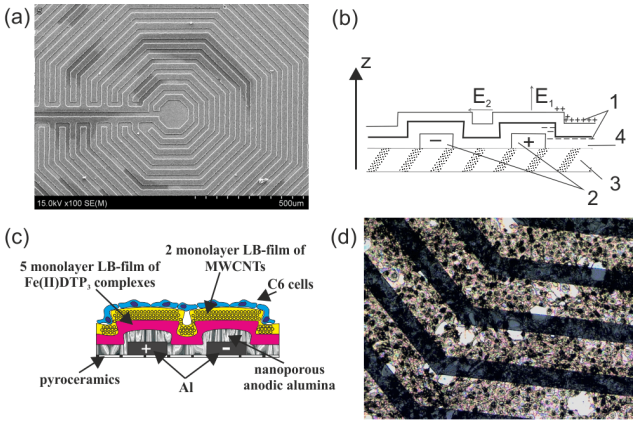

Fig. 2. (a) A SEM image of pure sensor. (b) A model of i -th "open type" capacitor: 1 – double electrically charged layer, 2 – positive and negative electrodes, 3 – dielectric substrate of sensor, 4 – dielectric barrier layer of AOA; E_1, E_2 are electric field strengths near the electrodes. (c) Scheme of fragment of sensor with sensitive MWCNTs-containing LB-coating and C6 cells. (d) A confocal microscopic image of rat C6 glioma cells grown on sensor surface coated by MWCNT-Fe-containing dithienylpyrrole LB-film.

To excite harmonic auto-oscillations of electric current (charge–discharge processes in the capacitors), the sensor was connected as the capacitance C into the relaxation RC-generator (self-excited oscillator) **[31]**. Operating of such RC-generators is based on the principle of self-excitation of an amplifier with a positive feedback on the quasi-resonance frequency. The capacitance C of the sensor entered in measuring RC-oscillating circuit has been calculated by the formula $C = 1/(2\pi Rf)$, where R is the measuring resistance, f is the frequency of quasi-resonance.

Structural and spectroscopy studies

Scanning electron microscopy (SEM) images were taken on LEO 1455 VP (Carl Zeiss, Gernamy) JEM-100CX. The accelerating voltage was 20 kV. Signals of reflected and secondary electrons were detected simultaneously. Microdiffraction patterns and transmission electron microscopic images were obtained by means of transmission electron microscope JEM-100CX (JEOL, Japan) (TEM) at accelerating voltage of 100 kV. After the objects were previously deposited on a copper grid with a formvar polymer coating, structural analysis has been performed.

Spectral studies in visible range were carried out using a confocal micro-Raman spectrometer Nanofinder HE ("LOTIS-TII", Tokyo, Japan-Belarus) by laser excitation at wavelength 532 nm with a power 20 mW. NMR

spectrometer "Bruker Avance 400", Germany was utilized in nuclear magnetic resonance (NMR) investigations.

Results and discussion

Structural and spectroscopic analysis

A TEM-image of the dried MWCNTs without non-covalent functionalization by stearic acid is shown in **Fig. 3a**. **Fig. 3b** demonstrates a low-intensive Raman spectrum of these MWCNTs. Raman spectra of graphene and graphene-like materials have been studied in detail (see **[32]** and references therein). The spectral bands *D* and *D*' in **Fig. 3b** reveal the existence of defects in graphene lattice and correspond to optical transverse and longitudinal in-plane vibrations in the vicinity of *K* point of the Brillouin zone. These phonons are nucleus oscillations in the field (term) of $\pi(p_z)$-electrons in valence band or π^*(d)-electrons in conduction band. The peak *D*" is a longitudinal acoustic mode in the vicinity of *K* point. The spectral band *G* originates also from in-plane carbon atoms vibrations, but in the electronic-vibrational term of sp^2-hybridized electrons. This resonance corresponds to optical surface phonons in the vicinity of *Γ* point of the Brillouin zone. D^3 and D^4 are transverse and longitudinal acoustic branches of in plane vibrations in the vicinity of *Γ* point. 2*D* is a peak of two phonon absorption (doubled *D* mode). Radial Breathing Mode (RBM) for MWCNTs is observed in frequency range from 60 to 430 cm^{-1}, as shown in **Fig. 3b**.

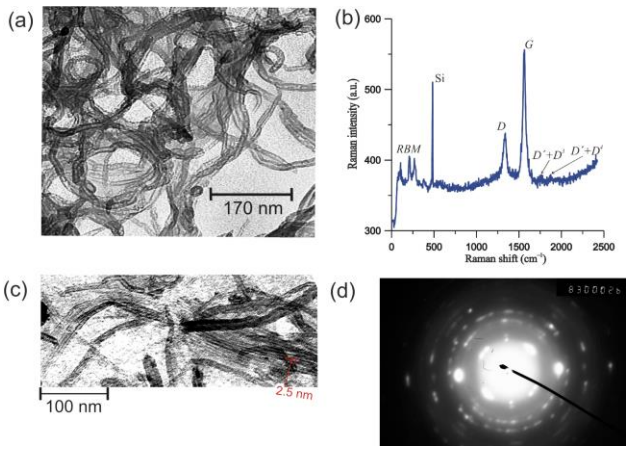

Fig. 3. (a) TEM-image of original carboxylated multi-walled CNTs. (b) Raman spectrum of original carboxylated MWCNTs on Si. (c) TEM-image of LB-MWCNT-bundle deposited on the Fe-containing dithienylpyrrole LB-film and microdiraction pattern (d) of two LB-monolayers of MWCNTs.

Diameters of MWCNTs can be estimated by RBM mode **[33**, **34]**. Calculations by RBM mode give the diameters of 2 nm for MWCNTs presented in our sample. According to a microdiffraction pattern in **Fig. 3d**, bundles of MWCNTs in the LB-film shown in **Fig. 3c** are high-ordered ones.

A Raman spectrum of $FeDTP_3$ presented in **Table 1a** has oscillations at 1342, 1348, 1410 and 1432 cm^{-1}, which are absent in the original H-dithienylpyrrole spectrum. These oscillations arise from Fe atom periodically leaving the ligand monolayer plane and coming back when changing the valence state of Fe atom from coordinate state II to III and vice versa. The assumption, that these oscillations are due to the mixed valence state of the metal center, is confirmed by the presence of high-frequency oscillation at 1432 cm^{-1} of thiophene ring in the Raman spectrum. Because of that, we call this oscillation as the oscillation of metal-center valence. Protonation of the LB films, placed in water, leads to shift of Raman bands into high-frequency region, for example, for 2-subst pyrrole Quadrant stretch from 1462 to 1472 cm^{-1} , according **Table 1a**. A Raman band 3436 cm^{-1} of NH is absent in the spectrum of $FeDTP_3$.

Results of ^1H, ^{13}C NRM-spectroscopy of H-dithienylpyrrole and LB-complex of Fe with H-DTP are shown in **Fig. 4** and **Table 1b**.

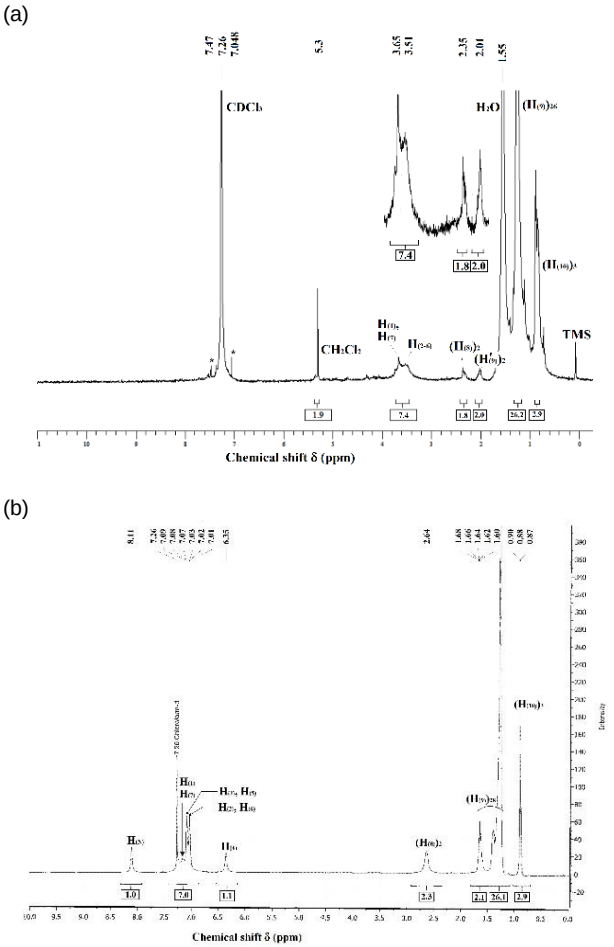

Fig. 4. ^1H NMR spectra (400 MHz, $CDCl_3$) of $FeDTP_3$ (a) and H-DTP (b).

The appearance of induced diamagnetic ring current in aromatic systems leads to de-screening of external protons of thiophene and pyrrole rings. Due to this fact, these protons are revealed in ^1H NMR spectrum of H-DTP at much weaker magnetic field in comparison with protons of alkyl chain. According to the NMR spectra, the number of protons in the alkyl chain is preserved after compression and formation of LB-films. The signals of aromatic protons, which are in the area of screening of diamagnetic ring currents in the heteroaromatic subsystems of neighboring molecules, are shifted to the

strong-field region at approaching of the molecules **[43**, **48**, **49]**. At that, the chemical shifts for thiophene and pyrrole protons are in the frequency bands with maxima at δ~3.65 and 3.51. Integrated intensities of a signal in lines shown in **Fig. 4** give a number of aromatic protons equal to 7 that is in agreement with the data of Raman spectroscopy and indicates the formation of macrocyclic dithienylpyrrole complex with Fe at substitution of hydrogen atom bounded with N. Line of the protons H_8 (δ~2.64) shifts also to the strong-field region from δ~2.35 due to approach of molecules when the metalloorganic complex forming. The stretched conformation of the alkyl chain $(CH_2)_{14}$ decreases the screening effect in comparison with coil, and the line of some protons H_9 (δ~1.64) shifts to the weak-field region at δ~2.01. Fe(II) forms a dome-shaped octahedral complex with ligands by S in the absence of H at N. Therefore, the organometallic LB-complexes film, on whose surface the MWCNT containing monolayers have been deposited as shown in **Fig. 3c**, decorates MWCNTs by the monolayer of the high-spin Fe atoms. Further we shall demonstrate that it makes MWCNTs to be able to screen an electromagnetic field.

Screening effects

Screening of electrically charged double layer by metal- and MWCNTs-containing LB-monolayers in water

The near-electrode double electrically charged layer is similar to plane capacitor. Because of a distance between plates of such capacitor is very small, its electric field strength is high. A high value of low-frequency dielectric permeability of water is due to ionization of water molecules and impurities in water with subsequent formation of hydrated complexes of ions OH^-, H^+ and of impurity ions.

Table 1a. Characteristic molecular vibrations, observed in the Raman spectra of 5-, 7- monolayers $FeDTP_3$ using 532 laser line, and of H-DTP using 785 laser line.

Band center for $FeDTP_3$ (cm^{-1})	**Band center for H-DTP (cm^{-1})**	**Region for vibration of similar molecular group (cm^{-1})**	**Assignment**	**Reference**
556	556	525	ring in-plane deformation	**[35]**
653	653	586	ring in-plane deformation	**[35]**
686	686	686	thiophene ring in-plane deformation	**[36 p. 64]**
741	741	750-690	C-S in thiophene	**[36 p. 64]**
804	805	808, 990-700	thiophene ring in-plane deformation	**[35], [37 p. 58]**
Shoulder at	844	844	thiophene ring	**[38]**
893	906	893, 990-700	trans hexadecyl-chain vibration, thiophene ring	**[39 p.118], [37 p. 58]**
1080, 1138	1080, 1138	1063	hexadecyl-chain trans C–C–C out-of-phase stretches	**[39 p.140, p.154]**
1158		1148	Cl–O vibration	**[36, 39 p.170]**
1231	1231	1236	CH bending	**[35]**
1310	1310	1310	inter-ring C–C vibration	**[40]**
1342		1357	semi-circle stretch of thiophene ring	**[39, p. 98]**
1348		1361–1345	2-subst thiophene Semi-circle stretch	**[39 p.109]**
1410		1420–1400	2-subst pyrrole Semi-circle stretch	**[39 p.98]**
1432		1455–1430	2-subst thiophene Quadrant stretch	**[39 p.98]**
1462*, 1472**	1468	1475–1460	2-subst pyrrole Quadrant stretch	**[39 p.98]**
1515	1540	1514–1540	2-subst thiophene Quadrant stretch	**[39 p.98]**
1586		1585–1607	C=C stretching in pyrrole rings	**[40]**
2940	2939	2940–2915-	CH_2 in alkanes	**[38 p.4]**
	3436	3440-3400	N-H in pyrrole	**[38 p.36]**

*, ** – measurements of samples have been performed in air and water, respectively.

Table 1b. The ranges of chemical shifts δ in ^{1}H, ^{13}C NMR spectra (400 MHz, $CDCl_3$) of $FeDTP_3$ and H-DTP.

^{1}H-NMR band for $FeDTP_3$, (ppm)	**^{1}H-NMR band for H-DTP, (ppm)**	**^{1}H-NMR chemical shift δ for similar molecular group (ppm)**	**^{13}C-NMR band for H-DTP (ppm)**	**Region for ^{13}C-NMR band of similar molecular group (ppm)**
0.879 ($3H_{10}$)	0.88 (m, $3H_{10}$)	0.8-1.1 for -CH_3**;** 0.88 (m, 3H) for 3-nonyl-2-(2-thienyl) pyrrole **[1]**.	14.3 (C_{10})	0-35 for **C**H_3-R
1.254–2.01 (m, $28H_9$), 2.35 ($2H_8$)	1.25–1.64 (m, $28H_9$), 2.64 ($2H_8$)	0.9-1.6 for -CH_2-**;** 1.4-1.24 (m, 14H, CH_2) and 2.69 (m, 2H, CH_2) for 3- nonyl-2-(2-thienyl) pyrrole **[41]**.	23, 27, 29.7, 29.86, 30.9, 32.08 ($14C_9$, C_8).	15-45 for R-**C**H_2-R, 20-70 for R-**C**H-R_1
3.51 (1H, H_4)	6.35 (1H, H_4)	6.10 (m, 2H, $H_{4,4'}$) for 2,5-dithienyl-1H-pyrrole **[42];** 6.84 (d, 2H, H4&H4') for 1-(bensonitryl)-2,5-di(2-thienyl)-1*H*-pyrrole **[44]**;	109.21 (C_4)	δ~ 104-116 for =CH- in pyrrole **[43 p.109]**
–	8.11 (1H, NH)	8.0(s, 1H, NH) for 2,5-di-(2-thienyl)-pyrrole **[4 p.119-130];** 8.08(s, 1H, NH) for 3-nonyl-2-(2-thienyl) pyrrole **[41];** 8.52 (s, 1H, NH) for 2,5-dithienyl-1H-pyrrole **[42];** >NH of heteroaromatic compounds, broadened band **[45 p.37, 39.]**	–	–
3.65 (2H, H_1 H_7), 3.51 (H_2–H_6)	7.12–7.01 (H_1–H_3, H_5–H_7)	7.66 (d, 2H, H1&H7), 7.36 (d, 2H, H2&H6), 7.13 (d, 2H, H3&H5), 6.84 (d, 2H, H4&H4') for 1-(bensonitryl)-2,5-di(2-thienyl)-1*H*-pyrrole **[44];** 6.2(d, 2H, H1&H7), 6.8(m, 6H, H1-H3&H5-H7&H4&4') for 2,5-di-(2-thienyl)-pyrrole **[4 p. 119-130];** δ: 7.2 (dd, 1H, H1), 7.05 (dd, 1H, H2), 6.98 (dd, 1H, H3), 6.16 (m, 1H, H4), for 3- nonyl-2-(2-thienyl) pyrrole **[41];** 7.39 (m, 2H, H1, H7), 7.07 (m, 2H, H3, H5), 6.89 (m, 2H, H2, H6) for 2,5-dithienyl-1H-pyrrole **[42]**.	127.86 ($3C^*_{pyr}$), 127.64 ($2C^*_{thio}$), 124.65 (C1, C7), 123.5 (C3), 122.74 (C5), 120.99 (C2, C6)	142.41, 133.96, 132.91, 130.59, 129.66, 127.13, 125.52, 125.05, 118.11, 112.5, 111.21 for 1-(bensonitryl)-2,5-di(2-thienyl)-1*H*-pyrrole **[44]**; 145.2 ($2C^*_{pyr}$), 143.23 ($2C^*_{thio}$), 131 (C1, C7), 127.8 (C3, C5), 115.3 (C2, C6), 113.5 (C4, C4') **[42]**.
1.55	–	H_2O **[46]**	–	–
7.048, 7.47	–	satellite lines δ=7.26 for $CDCl_2$ **[47]**	–	–

* – NMR lines corresponding to ^{13}C, which does not bond with hydrogen

The existence of such complexes impedes the ion recombination. One observes a resonance in frequency range from 200 to 600 kHz (curves 0 in **Fig. 5a**). The resonance occurs at an eigen frequency of hydrated-complex oscillations (ion vibrations) and causes a drop in the capacity value at the resonant frequency. The process of decay of hydrated complexes and, respectively, subsequent recombination of ions into neutral molecules H_2O results in decreasing of dielectric permeability of the medium.

As the conducting Fe-containing dithienylpyrrole LB-films add their free charged carriers to the electrical density of near-electrode layer, a screening effect is observed (curves 1 in **Fig. 5a**). This screening effect is stipulated by a surface plasmon resonance, which is mediated by the ion resonance and which enhances the sensor response to the ion recombination process in the electrically charged double layer (see Supplemental Information I). The density of charge carriers in the double electrically charged layer, which is not modified by the ultra-thin LB-film, is moderate one **[31]** because this resonance is observed as a wide band in dielectric spectrum with maximum in the range 200–600 kHz.

The large screening effect was observed at decoration of all surface of MWCNTs by the complexes of Fe(II) and Ce atoms (curves 2 in **Fig. 5a**), since the decorated MWCNTs possess non-zero electron density on the Fermi level. Because these screening effects, the probability of hydrated-complexes decay with subsequent recombination into neutral molecules increases sharply, narrowing the dielectric band with explicit extremum about 220 kHz for MWCNTs decorated by Fe(II) (curves 2 and insert in **Fig. 5a**) or 270 kHz for MWCNTs decorated by complexes of Fe(II) and Ce atoms being in mixing valence state also **[27]**. An addition of impurity ions Ce^{3+} into water decreases sharply the screening effect by LB-film with MWCNT decorated by Fe(II)DTP_3, because, as it is known **[1]**, the decoration with small doses of adsorbed atoms (adatoms) reduces and one with large doses suppresses the charge carrier mobilities of graphene devices.

As is known **[1]**, the distribution of adatom electron density near the graphene sheet causes a local spin-orbit field, and, respectively, the scattering of current components with positive (negative) angular momentum is enhanced (suppressed) for charge carriers with a spin projection $s_z = +1/2$ ($s_z = -1/2$). Furthermore, a spin-orbit splitting of the band dispersion occurs by bringing heavy metal atoms in close contact to graphene. Owing to the mixing valence of Ce and Fe, the charge carriers scattering in LB-monolayer of MWCNTs decorated by complexes of high-spin Ce and/or Fe(II) is spin-dependent. A vector of spin-dependent polarization of the LB-coating will precess in a magnetic field of the sensor. The spin precession is a quantum phenomenon consisting in an additional quantization of energy levels of a system in a magnetic field **[50]**. Dependencies of capacity upon ions concentration for the sensor, electrodes of which have been modified by the LB-coatings or remain unmodified, are represented in **Fig. 5b**. According to the experimental data, the LB-coatings screen an electric field of the near-electrode double layer, significantly decreasing the capacitance value and, therefore, not allowing appearance of break-down voltage. These dependencies have at least three inflection points. The stepwise dependence of the sensor capacity is due to a low-frequency Maxwell-Wagner polarization **[51, 52]** quantized by spin $\vec{S}$ orientation of the hydrate complexes of impurity radicals in a magnetic field of precessing spin of the plasmon-like mode in the spin-polarized LB-coating (see Supplemental Information II). A practically linear rise of the capacity occurs at increase in NaCl concentration in the range of physiological values (from 0.1 to 0.3 M) (**Fig. 5b**). Slope of the capacity dependence on [NaCl] in this concentration range varies with different types of LB-film. Let define a sensitivity S_{NaCl} of the sensor with the LB-coating as a magnitude of the sensor capacitance change per unit of NaCl concentration. As one can see in **Fig. 5c**, the sensor sensitivity in such a model system is practically not changed at deposition of MWCNT on Fe(II)DTP_3 complexes, but decorating of MWCNT with Ce-Fe(II)DTP_3 complexes results in significant increase of sensor sensitivity relative to [NaCl].

We estimated the sensor capacity change in different physiological mediums also. The minimal sensor capacity is observed for 0.15 M NaCl. If the sensor was immersed in Earle's medium (pH = 7.4) that does not contain $CaCl_2$, then its capacity increased by (100 – 200) pF and in Earle's medium with 2.5 mM $CaCl_2$ a further increase of capacity by (50 – 150) pF was observed. Thus, independently on ions composition of physiological medium the Maxwell-Garnett law is hold.

It was found out that the capacity of the sensor with LB-film from MWCNT-Fe(II)DTP_3 complexes in the Earle's medium is higher by 235 ± 95 pF (21 ± 4 %) than in 0.15 M NaCl while the capacity of this sensor in the Earle's medium is higher by 66 ± 11 pF (6,0 ± 0,5 %) than in Earle's medium without $CaCl_2$. The corresponding recordings for sensors with coating MWCNT decorated with Fe(II)-Ce DTP_3 complexes or Ce ions and Fe(II)DTP_3 complexes were 117 ± 27 pF (10,7 ± 0,5 %) and 80 ± 21 pF (8,2 ± 0,5 %).

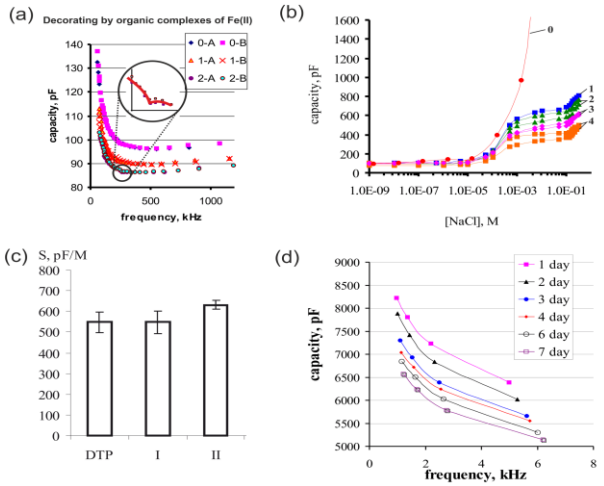

Fig. 5. (a) Cyclic frequency dependencies of capacity for sensors without (0) and with dithienylpyrrole LB-films (1) and MWCNTs (2) in deionized water. A and B denote direct and reverse branches, respectively. (b) Concentration dependencies of the capacity of sensors without (0) and with Fe-containing dithienylpyrrolle LB-film (1) and MWCNTs: (2) MWCNT decorated by Ce and organic complexes of Fe, (3) MWCNT decorated by organic complexes of Fe, (4) MWCNT decorated by organic complexes of Ce and Fe. Measurements are carried out at frequency 150 kHz. (c) Sensitivity of sensors with different LB-coatings: DTP – Fe-containing dithienylpyrrolle LB-film, I – LB-film with MWCNT decorated by organic complexes of Fe, II – LB-film with MWCNT decorated by organic complexes of Ce and Fe. (d) Frequency dependencies of the sensor capacity with C6 cell monolayer at different days of growth.

So, the experimental data under consideration indicate that the sensor with proposed nanocomposite LB-coating remains in the electroactive state for salt solutions with a large ionic strength.

Biocompatibility

To estimate the biocompatibility of the sensor sensitive coatings, C6 glioma cells was cultured on a sensor surface within 1–4 days, after that the morphology of cells were studied by means of light microscopy. It has been found out that cells adhere both to the electrodes and to interelectrode space. Like the control cells, which were grown on a glass, the cells, which were grown on sensors coated with different types of LB-films, are star-shaped with a large number of processes and cell-cell contacts.

By means of fluorescence analysis with propidium iodide, we evaluated the viability of glioma cells grown on MWCNTs- and Ce-containing LB-films. It has been established that PI does not penetrate into the cells, and PI fluorescence intensity in cells cultured on LB-MWCNT-clusters is the same as in control cells grown on the glass, and is two orders of magnitude lower than PI fluorescence intensity in cells damaged with triton X-100. This demonstrates the integrity and viability of cells cultured on the studied LB-coatings.

During cells growth on LB-coatings, a progressive increase in monolayer density has been observed. As

shown in **Table 2**, the densities of cell monolayers, which were cultured on LB-DTP-film and on LB-film with MWCNT decorated by organic complexes of Ce and Fe within 24 hours, are significantly lower than in the control sample (cells grown on glass). This indicates a retardation of cell adhesion to LB-DTP-film and Ce-containing LB-film with MWCNTs. At second, third and fourth days of growth the adhered cells divide mitotically and the density of cell monolayer increases for LB-coatings of all types.

Table 2. The dependence of the cell monolayer density ρ on time of cell growth *t* on glass and different LB-coatings

Type of support	Cell monolayer density ρ, 1/mm^2			
	24 h	48 h	72 h	96 h
Glass (control)	27 ± 7	113 ± 15	379 ± 45	643 ± 65
LB-DTP-film	14 ± 3*	93 ± 11	273 ± 38*	405 ± 50*
LB-film with MWCNT decorated by organic complexes of Fe	17 ± 5	88 ± 12	301 ± 30	598 ± 68
LB-film with MWCNT decorated by Ce and organic complexes of Fe	20 ± 4	52 ± 9*	284 ± 33*	390 ± 60*
LB-film with MWCNT decorated by organic complexes of Fe and Ce	14 ± 2*	80 ± 15	311 ± 40	637 ± 67

* - statistically significant in comparison with control, $p < 0.05$

At the same time, proliferative activity of cells cultured on LB-DTP-film and on LB-film with MWCNT decorated by Ce and organic complexes of Fe decreases, and the density of cell monolayer at 72 and 96 hours of cell growth is 30 - 40% lower than in the control samples. The proliferative activities of the cells on LB-film with MWCNT decorated by organic complexes of Fe and on LB-film with MWCNT decorated by organic complexes of Ce and Fe are the same as in the control sample. Thus, one can conclude that LB-films with MWCNT decorated by the organic complexes of Fe or the complexes of Fe and Ce possess good biocompatibility and can be used to detect electric impedance of cell monolayer.

Screening by living cell monolayers

A screening by living cell monolayer appears as cellular monolayer capacity C_{cell} decreasing on 1–7 days of cell growth (**Fig. 5d**) and it is partially stipulated by a formation of GJCs (**Fig. 6a**). It has been established that the capacity of the sensor with living cell monolayer is dependent on ions composition of the mediums and this dependence behaves inversely in comparison with the sensor without cells, notably the capacity of sensor with cell monolayer persistently decreases at its replacement from 0.15 M NaCl to 0.15 M NaCl plus 2.5 mM $CaCl_2$, then to the Earle's medium without $CaCl_2$, then to the Earle's medium. These facts indicate the dependence of the cellular monolayer capacity C_{cell} on functional state of the cells. It is known **[5-9]** that glucose and ions Ca^{2+} transport between cells in monolayer occurs through GJCs.

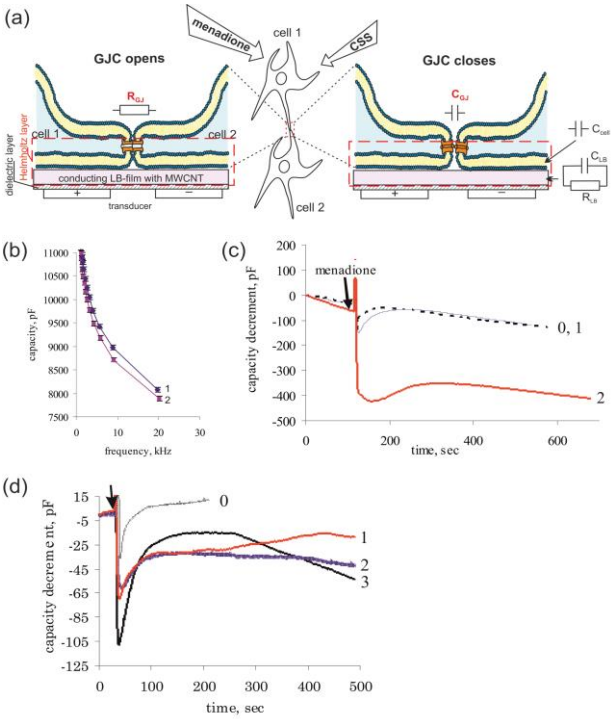

Fig. 6. (a) Principle of CGJC network activity detection by means of the impedance analysis. (b) Frequency dependencies of sensor capacity with C6 cell monolayer before (2) and after (1) 3 h treatment of gap junction inhibitor (0.1 mM carbenoxole sodium salt, CSS) (c) Kinetic dependencies of the capacity decrement of sensors at action of 10 μM menadione: (0) sensor without cells; (1) sensor with C6 cell monolayer treated with carbenoxolone sodium salt for 3 h. (2) sensor with C6 cell monolayer; (d) Kinetic dependencies of capacity decrement of sensors with different LB-films and C6 cell monolayer at action of DMSO (0, control) or 10 μM menadione: (1) LB-film with MWCNT decorated by Ce and organic complexes of Fe; (2) LB-film with MWCNT decorated by organic complexes of Ce and Fe; (3) LB-film with MWCNT decorated by organic complexes of Fe.

Therefore, one can assume that the screening (capacity decrease in **Fig. 5d**) is, at least partially, due to a phenomenon of CGJC network activity (GJCs opening/closing) which is detected as a change reactive component of impedance in **Fig. 6a**.

Further, we will reveal characteristic features of intercellular contact network functioning in the cellular monolayer. The gap junction inhibitor CSS, disrupting gap junction channels and preventing intercellular communication, leads to the increase of the capacity C_{cell} (**Figs. 6a, b**). It proves our assumption that the capacity C_{cell} decrease during cell growth is partially caused by opening of GJCs. On the contrary to CSS, the addition of menadione decreases the capacity C_{cell} on 400 pF, while its addition to the cellular monolayer with completely uncoupled GJC network does not change the sensor capacity (**Figs. 6a**, **c**). It indicates that menadione action on untreated cells induces the GJCs opening and, correspondingly, leads to the screening effect which observed as additional decrease of C_{cell}. Pattern of the cellular response to menadione treatment allows to suppose that menadione does not participate in self-assembly processes, rather changes a functional states of gap junction channels.

The kinetic dependencies of the capacity C_{cell} at menadione addition to cellular monolayer grown on LB-coatings of different types were recorded (**Fig. 6d**). As on can see, the maximum of the capacity decrement after the menadione addition is lower for Ce-containing LB-films, while in 100-200 s intervals the capacity of sensor with Ce-containing LB-films is less than for MWCNT decorated by the complexes Fe(II)DTP_3.

It is known that Ca^{2+} is important for intercellular communication, while Ce^{3+} can inhibit calcium channels **[53]**. The analysis of the obtained data allows to suppose that the menadione treatment results in opening of gap junction channels following the opening of the calcium channels with subsequent suppression of GJIC. The calcium channels is partially inhibited in the cells grown on MWCNTs decorated by complexes Fe(II)-CeDTP_3 and on MWCNTs decorated by Ce ions and Fe(II)DTP_3 complexes that leads to failure of GJIC regulation.

Table 3 presents a comparison of the constructed nanobiosensor with some previously reported ones. As one can see, a biosensor which is able to provide GJIC detection has not been developed before. Conventional ECIS biosensors are faradeic biosensors which are effective detectors of number of cells adhered on sensor surface that allowed to propose a different design to estimate cell proliferation, migration or cell-cell tight-junctions formation. The faradeic sensors operate at nanoF range of capacity values. This does not allow to detect weakest changes in the intercellular ions currents provided by intercellular communication. On the other hand, a nonfaradeic-sensor operation is in detection of changes in a surface charge distribution. Because of this, the nonfaradeic sensor is potentially very sensitive to interfacial change, namely to change of the electrical double layer capacitance. Nonfaradeic biosensors can detect changes up to 1-2 pF. However, an improvement of such sensor sensitivity is a challenge. As one can see from **Table 3**, immobilization of bacteria on the sensor surface led to an increase of the capacity only in about 30 pF.

Table 3. Comparison between our nanobiosensor and other impedance based cell biosensors.

Biosensor	**Type of biosensor**	**Adhesive layer/ electrode**	**Cell type**	**Estimated parameters**	**Change of capacity between free sensor and sensor with confluent monolayer**	**Capacity detection limit**	**Ref**
Our nanobiosensor	nonfaradaic	LB-DTP-MWCNT-film / AOA-coated Al	rat C6 glioma	Cell proliferation Cell attachment Gap-junction intercellular communication	~2 nF	~2 pF	Our study
conventional ECIS	faradaic	Pt or Au (for both purposes)	LS 174T colorectal adenocarcinoma	Cell proliferation Cell migration Cell attachment	~200 nF	~10 nF	**[54-56]**
ECIS sensor with conducting polymer coating	faradaic	Polypyrrole/Au	16-HBE epithelial cell line	Cell proliferation Cell-cell tight-junctions formation	~2000 nF	~10 nF	**[57]**
whole-cell based capacitive biosensor	nonfaradaic	3-mercapto-propionic acid layer/Au	Immobilized living E. coli	Number of cells Shape of cells	~30 pF	~2 pF	**[58]**

Proposed by us, the sensitive coating from MWCNTs decorated by DTP-complexes of Ce and/or Fe(II) realizes the idea of the surface enhancement of the polarization response and, consequently, enhancement of nanobiosensor sensitivity to the double layer capacitance changes. Due to this phenomenon, the capacity decrease at the confluent cell monolayer formation is as high as 2 nF, and also the

changes of the double layer provided by GJIC has been detected.

Conclusion

Summarizing our results, it has been found out that MWCNTs, decorated by organometalic complexes of high-spin Fe(II), efficiently screen the double electrically charged layer in the near-electrode region. MWCNTs decorated by Fe(II)DTP_3 complexes or by Fe(II)-Ce DTP_3 complexes are biocompatible and stable in the physiological mediums. The proposed capacitive sensor based on the spin-dependent polarization effects has been used to detect phenomena of CGJC-network activity in real-time.

Acknowledgements

This study was supported by grants from the Ministry of Education and National Academy of Science, Republic of Belarus.

Author's contributions

Conceived the plan: HVG; Performed the expeirments: HVG, NGK, IVL, TIO, BGS; Data analysis: HVG, NGK, IVL; Wrote the paper: HVG, NGK. Authors have no competing financial interests.

Supporting information

Supporting informations are available from VBRI Press.

References

1 Ferreira, T.G.; Rappoport, M.A.; Cazalilla, A.H.; Castro, N.; *Phys. Rev. Lett.*, **2014**, *112*, 066601. **DOI:** 10.1103/PhysRevLett.112.066601
2 Sun, H.; Wu, L.; Wei, W.; Qu, X.; *Mater. Today*, **2013**, *16*, 433. **DOI:** 10.1016/j.mattod.2013.10.020
3 Lu, S.; Chen, Z.W.; Li, C.; Li, H.; Zhao, Y.F.; Gong, Y.Y.; Niu, L.; Liu, X.; Wang, T.; Sun, C.Q.; *J. Mater. Chem. A*, **2016**, *4*, 14827. **DOI**: 10.1039/C6TA06628C
4 Arsalani, N.; Goganian, A.M.; Kiani, G.R.; Hosseini, M.G.; Entezami, A.A. Electrosynthesis and Characterization of Polypyrrole in the Presence of 2,5-di-(2-thienyl)-Pyrrole (SNS), In Electropolymerization; Schab-Balcerzak E. (Ed.); InTech: Rijeka, Shanghai, **2011**, pp.119-130. **DOI:** 10.5772/31745
5 Kurtenbach, S.; Kurtenbach, S.; Zoidl, G.; *Front. Physiol*., **2014**, *5*, 82. **DOI:** 10.3389/fphys.2014.00082
6 Mese, G.; Richard, G.; White, T.W.; *J. Invest. Dermatol*., **2007**, *127*, 2516. **DOI:** 10.1038/sj.jid.5700770
7 Salameh, A.; Dhein, S.; *Biochim. Biophys. Acta*, **2005**, *1719*, 36. **DOI:** 10.1016/j.bbamem.2005.09.007
8 Dere, E. (Ed.); Gap Junctions in the Brain; Elsevier: Amsterdam, **2013**.
9 Moinfar, Z.; Dambach, H.; Faustmann, P.M.; *Front.Physiol*., **2014**, *5*, 186. **DOI:** 10.3389/fphys.2014.00186
10 Klotz, L.O.; Hou, X.; Jacob, C.; *Molecules*, **2014**, *19*, 14902. **DOI:** 10.3390/molecules190914902
11 Abbaci, M.; Barberi-Heyob, M.; Blondel, W.; Guillemin, F.; Didelon, J.; *BioTechniques*, **2008**, *45*, 33. **DOI:** 10.2144/000112810
12 Delachei, P.; Double layer and kinetics of electrode processes; Mir: Moscow, **1967**.
13 Chelidze, T.L.; Derevjanko, A.I.; Kurilenko, O.D.; Electric spectroscopy of heterogenous systems; Naukova dumka: Kiev, **1977**.
14 Bonincontro, A.; Risuleo, G.; *Adv. Mol. Imaging*, **2015**, *5*, 1. **DOI:** 10.4236/ami.2015.51001
15 Xu, Y.; Xie, X.; Duan, Y.; Wang, L.; Cheng, Z.; Cheng, J.; *Biosens. Bioelectron*., **2016**, *77*, 824. **DOI:** 10.1016/j.bios.2015.10.027
16 Hong, J.; Kandasamy, K.; Marimuthu, M.; Choi, C.S.; Kim, S.; *Analyst (Cambridge, U.K.)*, **2011**, *136*, 237. **DOI:** 10.1039/c0an00560f
17 Srinivasaraghavan, V.; Strobl, J.; Wang, D.; Heflin, J.R.; Agah, M.; *Biomed. Microdevices*, **2014**, *16*, 689. **DOI:** 10.1007/s10544-014-9873-1
18 de Leon, C. P.; Campbell, S.A.; Smith, J.R.; Walsh, F.C.; *Trans. Inst. Met. Finish*., **2008**, *86*, 34. **DOI:** 10.1179/174591908X264392
19 Zomer, P.J.; Guimarres, M.H.D.; Tombros, N.; van Wees, B.J.; *Phys. Rev. B*, **2012**, *86*, 161416. **DOI:** 10.1103/PhysRevB.86.161416
20 Morozov, S.V.; Novoselov, K.S.; Geim, A.K.; *Phys. - Usp.*, **2008**, *178*, 776. **DOI:** 10.3367/ufnr.0178.200807i.0776.
21 Grushevskaya, H.V.; Krylov, G.; *J. Nonlin. Phen. in Complex Sys*., **2014**, *17*, 86.
22 Grushevskaya, H.V.; Krylov, G.G. Graphene: beyond the massless Dirac's fermion approach, In Nanotechnology in the Security Systems, NATO Science for Peace and Security Series C: Environmental Security; Bonča J.; Kruchinin S. (Eds.); Springer Science+Business Media, Dordrecht, **2015**, pp. 21-31. **DOI:** 10.1007/978-94-017-9005-5_3
23 Semenkova, G.N.; Hrushevsky, V.V.; Krylova, H.V.; Krylova, N.G.; Kulahava, T.A.; Lipnevich, I.V.; Orekhovskaya, T.I.; Shulitsky, B.G.; *J. Nonlin. Phen. in Complex Sys.*, **2011**, *14*, 295.
24 Grushevskaya, H.V.; Krylova, N.G.; Lipnevich, I.V.; Orekhovskaya, T.I.; Egorov, A.S.; Egorova, V.P.; Govorov, M.I.; Kulahava, T.A.; Semenkova, G.N.; Shulitsky, B.G.; Ulashchik, V.S.; Vasiljev, N.V.; *Proc. NAP*., **2013**, *2*, 04NABM22.
25 Labunov, V.; Shulitski, B.; Prudnikava, A.; Shaman, Y.P.; Basaev, A.S.; *SPQEO*, **2010**, *13*, 137. **DOI:** 10.15407/spqeo13.02
26 Kel'in, A.; Kulinkovich, O.; *Folia pharm. Univ. Carol.* (supplementum), **1995**, *18*, 96.
27 Grushevskaya, H.V.; Lipnevich, I.V.; Orekhovskaya, T.I.; *J. Mod. Phys*., **2013**, **4**, 7. **DOI:** 10.4236/jmp.2013.412A3002
28 Hurski, L.I.; Krylova, H.V.; Lipnevich, I.V.; Kozyrkov, Y.Y.; Orechovskaja, T.I.; BY Patent 19933 C2, **2015**.
29 Grushevskaya, H.V.; Krylova, N.G.; Lipnevich, I.V.; Orekhovskaja, T.I.; Egorova, V.P.; Shulitski, B.G.; *Int. J. Mod. Phys. B*, **2016**, *30*, 1642018. **DOI:** 10.1142/S0217979216420182
30 Egorov, A.S.; Krylova, H.V.; Lipnevich, I.V.; Shulitsky, B.G.; Baran, L.V.; Gusakova, S.V.; Govorov, M.I.; *J. Nonlin. Phen. in Complex Sys*., **2012**, *15*, 121.
31 Abramov, I.I.; Hrushevsky, V.V.; Krylov, G.G.; Krylova, H.V.; Lipnevich, I.V.; Orekhovskaya, T.I.; *Petersburg J. Electronics*., **2012**, *4(73)*, 59.
32 Cooper, D.R.; D'Anjou, B.; Ghattamaneni, N.; Harack, B.; Hilke, M.; Horth, A.; Majlis, N.; Massicotte, M.; Vandsburger, L.; Whiteway, E.; Yu, V.; *ISRN Condens. Matter Phys*., **2012**, *2012*, 56. **DOI:** 10.5402/2012/501686
33 Fantini, C.; Jorio, A.; Souza, M.; Strano, M.S.; Dresselhaus, M.S.; Pimenta, M.A.; *Phys. Rev. Lett*., **2004**, *93*, 147406. **DOI:** 10.1103/PhysRevLett.93.147406
34 Souza Filho, A.G.; Chou, S.G.; Ge, G.S., Dresselhaus, G.; Dresselhaus, M.S.; An, L.; Liu, J.; Swan, A.K.; Ünlü, M.S.; Goldberg, B.B.; *Phys. Rev. B*, **2004**, *69*, 115428. **DOI:** 10.1103/PhysRevB.69.115428
35 Constantino, C.; Duff, J.; Aroca, R.; *Spectrochim. Acta, Part A*, **2001**, *57*, 1249. **DOI:** 10.1016/S1386-1425(00)00470-4
36 Nakanishi, K.; Infrared Spectra and Organic Compounds Structure; Mir: Moscow, **1965**.
37 Brown, D.W.; Floyd, A.J.; Sainsbury M. Spectroscopy of Organic Substances; Mir: Moscow, **1992**.
38 Tarasevich, B.N.; IR-Spectra of Basis Classes of Organic

Compounds; MSU: Moscow, **2012**.
39 Larkin, P.; Infrared and Raman Spectroscopy: Principles and Spectral Interpretation; Elsevier: Oxford, **2011**.
40 Santos, M.J.L.; Brolo, A.G.; Girotto, E.M.; *Electrochim. Acta*, **2007**, *52*, 6141.
DOI: 10.1016/j.electacta.2007.03.070
41 Trofimov, B.A.; Mikhaleva, A.I.; Schmidt, E.Yu.; Ivanov, A.V.; Zorina, N.V.; Protzuk, N.I.; RU Patent 2477725, **2013**.
42 Oberoi, S.; Synthesis and Characterization of Thin Films of Novel Functionalised 2,5-Dithienylpyrrole Derivatives on Oxide Substrates; Dissertation; Dresden University of Technology: Dresden, **2005**.
43 Nifant'ev, I.E.; Ivchenko, P.V.; Practical Practical Course in Nuclear Magnetic Resonance Spectroscopy; MSU: Moscow, **2006**.
44 Kim, Y.H.; Hwang, J.; Son, J.; Shim, Y.; *Synth. Met*., **2010**, *160*, 413.
DOI: 10.1016\j.synthmet.2009.11.021
45 Pouchert, Ch. J. (Ed.); The Aldrich Library of Infrared Spectra.; Aldrich Chemical Company: Milwaukee, Wisconsin, **1983**.
46 Pretsch, E.; Büllmann, P.; Affolter, C.; Structure Determination of organic compounds. Tables of spectral data; Springer-Verlag: Berlin, **2000**.
47 Ashutosh Tiwari, Anthony PF Turner (Eds), Biosensors Nanotechnology, John Wiley & Sons, USA, **2014**.
48 Smith, K.M. (Ed.); Porphyrins and Metalloporphyrins; Elsevier: Amsterdam, **1975**.
49 Smith, K.M. Nitrogen-Containing Heterocycles, In Comprehensive Organic Chemistry, *Vol. 8*; Barton D.H.R.; Ollis W.D. (Eds.); Pergamon: Oxford, 1979.
50 Fock, V.A.; Principles of Quantum; Mechanics Science: Moscow, 1976.
51 Hrushevski, V.; Krylov, G.; Krylova, H.; Lipnevich I.; Orechovskaja, T.; *Vestnik BSU. Series 1: Phys. Math. Inform.Sci.*, **2012**, 2, 23.
52 Vinogradov, A.; Electrodynamics of Composite Materials, URSS: Moscow, **2001**.
53 Lansman, J.B.; *J. Gen. Physiol*., **1990**, *95*, 679.
54 Ehret, R.; Baumann, W.; Brischwein, M.; Schwinde, A.; Wolf, B.; *Med. Biol. Eng. Comput.*, **1998**, *6*, 365.
55 Ehret, R.; Baumann, W.; Brischwein, M.; Schwinde, A.; Stegbauer, K.; Wolf, B.; *Biosens. Bioelectron.*, **1997**, *12*, 29.
56 Atul Tiwari, Ashutosh Tiwari (Eds), Bioengineered Nanomaterials, CRC Press, USA, **2013**.
57 Sun, T.; Swindl, E.J.; Collins, J.E.; Holloway, J.A.; Davies, D.E.; Morgan, H.; *Lab Chip*, **2010**, *10*, 1611. **DOI:** 10.1039/c000699h
58 Qureshi, A.; Pandey, A.; Chouhan, R.S.; Gurbuz, Y.; Niazi, J.H.; *Biosens. Bioelectron.* **2015**, *67*, 100.
DOI: 10.1016/j.bios.2014.07.038.

Supporting information

I. Surface-enhanced polarization response

A response of substance to an electric field $\vec{E}$ of sensor electrodes, to which a potential difference is applied (an applied bias *V*), is formed as a result of bulk dielectric polarization $\vec{P} = \vec{P}_0 + n\vec{d}$, where $\vec{P}_0$ is a vector polarization for water without any ions, $\vec{d}$ is an electric dipole moment of a hydrate complex, *n* is a density of hydrated ions. The alternative electric field $\vec{E}$ causes a resonant decay of hydrate complexes at eigenfrequencies of ion oscillations ω_{res}. The decay changes a number of hydrate complexes dipoles and, consequently, lowers the polarization magnitude up to a value $\vec{P}_{res} = \vec{P}_0 + m\vec{d}$, $n > m$. A contribution $(m-n)\vec{d}$ of the change into the electromagnetic field polarization response of the sensor is small due to a low ions concentration (**Fig. S1**).

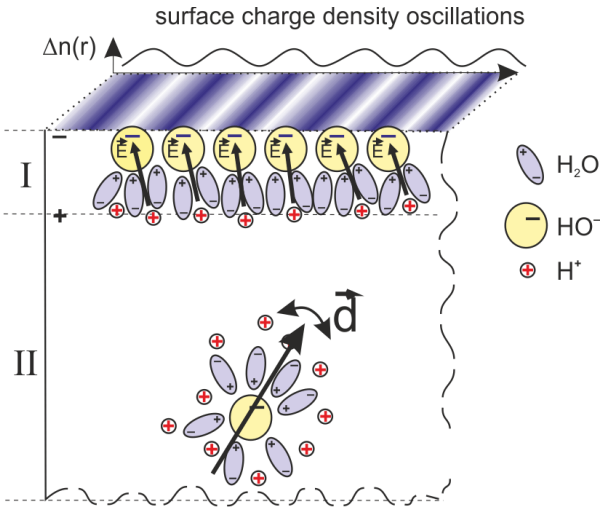

Fig. S1. Operation principles of a non-faradaic sensor to detect polarization processes in a Helmholtz electrically charged double layer. I, II denote areas of volume and surface polarization, respectively. A surface charge density $\Delta n(r)$ oscillates in resonance with vibrations of a dipole moment $\vec{d}$ a of hydrate complex.

Metallic surface states of a near-electrode layer resonate with the ions recombination process mediately through the ion resonance at the frequency ω_{res}. The surface states are excited by electromagnetic quanta emitted in the recombination process so that vibrational modes of surface charge density $\Delta n(r)$ are resonantly excited. These plasmon modes are in-elastically scattered on hydrated ions of Helmholtz electrically charged double layer (**Fig. S1**). A channel of the inelastically scattering is the hydrate complexes decay followed by the ions recombination. The surface-enhanced polarization response is registered by the sensor. Because of the high density of the hydrate complexes in the Helmholtz layer, their decay is expressed in a significant decrease of the surface contribution into an electric capacity at the frequency ω_{res}. The decrease in the double layer capacity is revealed as a screening of electrically charged double layer (**Fig. 5a**).

So, the constructed non-faradaic sensor operates in a range of the eigenfrequencies of hydrated-ion vibrations. The phenomenon of surface-enhanced inelastic scattering of ions in the hydrate complexes and the following phenomenon of surface-enhanced ions recombination ensure high performance of the sensor.

II. Quantized Maxwell–Wagner polarization

Halogens, particularly Cl, can participate in a hydration reaction, for example:

$$NaCl + n\,H_2O \leftrightarrows Na^{g}HO(H_2O)_{n-1} + H^{+}Cl^{g}, \qquad (S1)$$

where *n* is a number of molecules H_2O entering in the hydrate complex $Na^{g}HO(H_2O)_{n-1}$. An occurrence of unpaired electrons in the reaction (S1) leads to an emergence of a hydrate-complex spin $\vec{S}$. A scattering of electrons of MWCNTs and conducting $FeDTP_3$-film on atoms of rare earth and transition elements is spin-dependent one. The spin-dependent current of charge carriers produces a spin-dependent scattering of the surface-charge-density vibrational modes of plasmon type. The spin $\vec{S}$ of $Na^{g}HO(H_2O)_{n-1}$ is oriented in a magnetic field of precessing spin of the plasmon-like mode. Spin-orbital coupling leads to an appearance of discrete energy levels in electronic band structure, and hence, the polarization of hydrate complexes becomes discrete. The stabilization of $Na^{g}HO(H_2O)_{n-1}$ complexes enhances significantly a redox ability of the capacitive sensor.